Distance-Dependent Enhanced ENDOR Phase (DEEP) Spectroscopy and Its Application to Determination of Solvation Structure around Paramagnetic Ions in Disordered Solids: The Three Ordered Hydration Shells of Aquated Transition Ions

Ming Zheng and G. Charles Dismukes*

Department of Chemistry, Princeton University, Hoyt Laboratory, Princeton, New Jersey 08544

We present a method that improves the spectral resolution and extends the distance range for detection of ordered solvent molecules surrounding a paramagnetic ion in frozen solutions using ^{1}H electron−nuclear double-resonance (ENDOR) spectroscopy. This method is based on the R^{-3} distance dependence of the proton−electron spin hyperfine interaction and its effect on the electron−nuclear cross relaxation rate. This relaxation effect dramatically influences the ENDOR phase spectrum and appears through the radio-frequency (rf) phase angle dependence (using the conventional rf modulation detection scheme), and thus it is termed distance-dependent enhanced ENDOR phase (DEEP) spectroscopy. Applying DEEP spectroscopy to the conventional CW-ENDOR experiment, one is able to eliminate the large proton matrix peak from disordered solvent molecules. We observe a 4-fold increase in spectral resolution with DEEP spectroscopy for distant protons. When applied to solvation of aquo Mn(II) ions, we resolve ^{1}H hyperfine couplings from molecules in the first shell at 2.90 Å (Mn−H), two distinguishable groups of molecules in the second solvation shell at 4.37 and 5.05 Å, and a less-ordered third shell of protons at 7.5 Å. The structure in the second shell and the presence of the third shell of ordered water molecules are the first observations of this structure and are supported by previous molecular dynamics simulations of aquo Mn(II) ions in aqueous solutions [Sivaraja et al. *J. Am. Chem. Soc.* **1992,** *114,* 9600−9603]. DEEP spectroscopy holds promise for studies of solvation to other paramagnetic ions, including Gd(III) and those used as MRI contrast agents.

Introduction

Cation hydration in aqueous solution is a fundamental phenomenon in both chemistry and biology.[1,2] Hydration determines the transport and thermodynamic properties (dielectric constant, compressibility, entropy, etc.) of ions in aqueous solution. A well-known example is the selective transport of Na^+ vs K^+ ions in a living cell which is determined by the size and affinity of their hydration spheres.[3] With the increasing recognition of the importance of the ions and solvation in determining the conformation of bio-macromolecules and membranes, understanding the solvation structure of ions in disordered solutions has grown in significance.

The most direct and comprehensive experimental methods for determining hydration structure are X-ray and neutron scattering.[4−6] However, contributions to the diffraction pattern come from all local structures with short-range order, which include cation hydration structure, anion hydration structure, and water structure. To increase the relative contribution from the solute hydration shell structure to the total diffraction intensity, concentrated solutions (>1 M) are needed. Because solution concentrations encountered in aqueous chemistry and in a living cell are far below that used in scattering methods, the degree of relevance of the structural data derived from scattering methods is questionable. NMR of paramagnetic ions can sometimes be used to obtain quantitative information, but the relatively low sensitivity of NMR also requires high solution concentrations. EXAFS (extended X-ray absorption fine structure) spectroscopy is more sensitive than the above-mentioned methods and is able to reveal structural information on highly diluted solutions (ca. 10^{-3} M). Therefore, it was used in the determination of ion solvation structure extending into the second solvation shell.[7]

In contrast with the spectroscopic methods, studies based on ion transport and thermodynamic measurements work with dilute solutions, but they can yield only partial characterization of the hydration structure and require certain approximate assumptions. For instance, measurement of ionic mobilities measured in infinitely dilute solutions yields an estimate of the effective radii of the hydrated ions if the Stokes relation is used with certain calibrations.[8]

[1]H ENDOR of paramagnetic centers appears to be the method of choice in studying hydration structure of disordered paramagnetic ions and has been employed extensively.[9−12] It works with low solution concentrations (≥0.1 mM) and allows the determination of proton hyperfine interactions. The latter can be used for obtaining the distance between protons and the unpaired spin density, which can be used to deduce distances provided the unpaired spin density distribution within the spin system is measured or known. Applications to single crystals for which diffraction data are available have confirmed the high precision of the ENDOR method for determination of distances.[13] However, the ENDOR method is limited for disordered solutions to first and second shell solvation structure, owing to the loss of spectral resolution arising from increasingly disordered solvent molecules in the second and more distant hydration shells. Moreover, the spectral density from well-ordered nuclei exhibiting no disorder increases with distance from the paramagnetic center, since the number of protons in each shell increases roughly as R^2, while the dipolar part of the hyperfine interaction decreases as R^{-3}. The combined effects

Paramagnetic Ions in Disordered Solids

J. Phys. Chem. B, Vol. 102, No. 42, 1998 **8307**

of solvation disorder and increasing spectral density produce the broad "matrix peak" in ENDOR spectroscopy which limits resolution.

In the present work, a simple method commonly used in modulation spectroscopy for separating the in-phase and out-of-phase responses of a resonant system is applied to the ENDOR experiment. Because of the sensitive dependence of the out-of-phase signal response to the electron−nuclear cross relaxation rate, the out-of-phase response is exquisitely sensitive to distance. This sensitivity to distance enables discrimination of ENDOR transitions from different solvation shells. Using this approach, one is able to enhance selectively weak ENDOR transitions from distant ordered solvent shells relative to both inner solvent shells and also from disordered solvent molecules. The method permits enhanced resolution of the solvation structure within the second and third shells out to 7.5 Å from the paramagnetic divalent cation. As a test system for demonstration of this method, we have used aquo Mn(II) ions, but it is generally applicable to all paramagnetic ions with solvation by molecules possessing nuclear spins. Mn(II) was chosen because it has been extensively studied by EPR, ENDOR, and molecular dynamics simulations.[13−16]

Experimental Section

Sample Preparation. Aqueous solutions of Mn(II) were prepared by dissolving $MnCl_2 \cdot 4H_2O$ into 30% ethylene glycol/deionized water to a final concentration of typically 2 mM. Concentrations over the range 0.5−10 mM were examined in order to verify that the spectra scale linearly with concentration, implying no aggregation was occurring. Samples were also prepared using deuterated ethylene glycol (d_6, 99.7% from Cambridge Isotopes Lab).

EPR and ENDOR Spectroscopy. EPR and ENDOR measurements were done using Bruker spectrometers, ESP300 and ER250A, respectively. The standard Bruker ENDOR cavity (TM_{110}) and rf coil (16 turns, 0−30 MHz bandwidth) were used. The Bruker ENDOR detection system utilizes frequency modulation of the rf excitation source and subsequent phase-sensitive amplification. The rf modulation frequency was varied from 1.56 to 100 kHz. The maximum rf power from the amplifier (ENI model 3200L, 250 kHz to 150 MHz) was limited to 300 W using a 50 ohm load in series with the coil. Temperatures below 70 K were achieved using an Oxford ESR900 gaseous helium flow cryostat. The rf reference phase calibration was done at room temperature with PNT (phenalenyl radical) in mineral oil.

Signal Processing. To disentangle the ENDOR amplitude response from the phase response in a series of spectra taken at different lock-in reference phase settings, we adopted a signal processing technique used in various types of modulation spectroscopy, including saturation transfer EPR spectroscopy.[17] In this method, a series of n spectra are acquired at the instrumental phase angles, $X_i = (j - 1) \cdot 180/n$ (where $j = 1, 2, ..., n$). The experimental signal intensity induced by sinusoidal rf modulation at frequency f, given by $Y_i(f)$, is assumed to vary in a sinusoidal manner with respect to the instrumental phase setting, eq 1.

$$Y_i(f) = A(f) \cos[X_i - \theta(f)] \qquad (1)$$

where $A(f)$ and $\theta(f)$ are defined as the intrinsic amplitude and phase responses of the signal at resonance frequency f, also known as the power and phase spectra, respectively, for obvious reasons. Least-squares fitting of the experimental data to eq 1

yields expressions for $A(f)$ and $\theta(f)$, given by eqs 2 and 3, respectively.

$$A(f) = (2/n)\left\{\left[\sum_{i=1}^{n} Y_i(f) \cos X_i\right]^2 + \left[\sum_{i=1}^{n} Y_i(f) \sin X_i\right]^2\right\}^{1/2} \qquad (2)$$

Equations 2 and 3 essentially define the algorithm for

$$\theta(f) = \arctan \frac{\sum_{i=1}^{n} Y_i(f) \sin X_i}{\sum_{i=1}^{n} Y_i(f) \cos X_i} \qquad (3)$$

obtaining the power and the phase spectra numerically. For this purpose we used a commercial program called VEPR (for vector EPR; Bruker Instruments). In a typical experiment we use an automated data acquisition routine that automatically increases the reference phase in the $0°−180°$ region with a predefined increment. A series of ENDOR spectra obtained at different instrument phase settings are baseline corrected and then input directly into the VEPR program to yield the corresponding power and phase spectra.
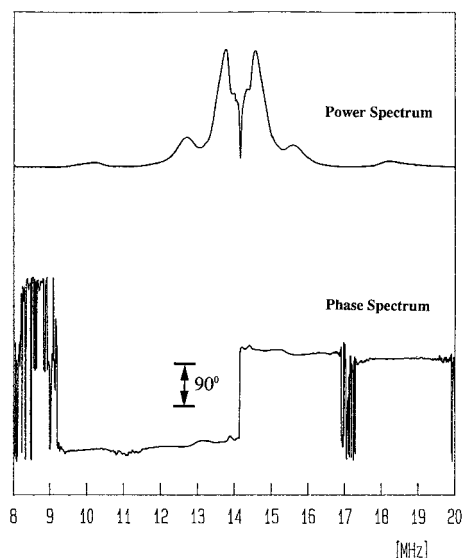
Results

Solvent Effects. In prior work from this laboratory we reported that the 100-fold loss of EPR intensity that occurs upon freezing of aqueous solutions of Mn^{2+} salts to form microcrystalline powders can be eliminated by use of a low pH (<1) achieved by addition of noncoordinating acids (e.g., $HClO_4$).[14] The loss of intensity upon freezing of *unacidifed* solutions can be ascribed to low-symmetry environments around Mn(II) that have zero-field splittings (zfs), which broadens the EPR signal. It was hypothesized that noncoordinating acids suppress the freezing-induced loss of EPR (and ENDOR) intensity by suppressing formation of low-symmetry strong ion pairs ($Mn^{2+}\cdots Cl^-$) by higher-symmetry weak ion pairs ($Mn^{2+}\cdots ClO_4^-$) and/or by movement of Mn^{2+} ions away from the ice grain boundaries where electrical field gradients would increase the zero-field splittings.

The same effect is seen if perchloric acid is replaced by 30% ethylene glycol, a well-known cryoprotectant solvent system which induces glass formation. Concentrations lower than 30% ethylene glycol lead to microcrystalline samples which exhibit the same degree of loss in EPR signal intensity. Importantly, the six-line aquo Mn(II) EPR signal at ~4 K observed in the glassy ethylene glycol solutions saturates at appreciably lower microwave power ($P_{1/2}$ at least 6 dB lower) than that for Mn(II) in acidic solutions without cryoprotectant (data not shown). The resulting ^1H ENDOR signal obtained from Mn(II) ethylene glycol solution is at least 10 times stronger than obtained in acidified frozen powders, reflecting the strong dependence of the ENDOR effect on the spin relaxation rate. The origin of the slower spin relaxation rate in glassy solutions may be associated with the greater homogeneity of the Mn(II) environment.

Rf Phase Dependence. When the standard PNT sample is measured at room temperature, it exhibits a normal phase behavior at low rf modulation frequencies with the signal intensity changing sinusoidally with respect to the reference phase and exhibits a maximum when in-phase and zero at 90° out of phase. (In our spectrometer this occurs at 130° and 310° and 40° and 230°, respectively, when the frequency modulation
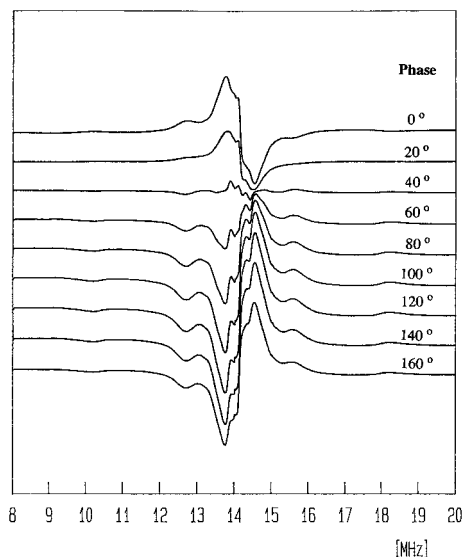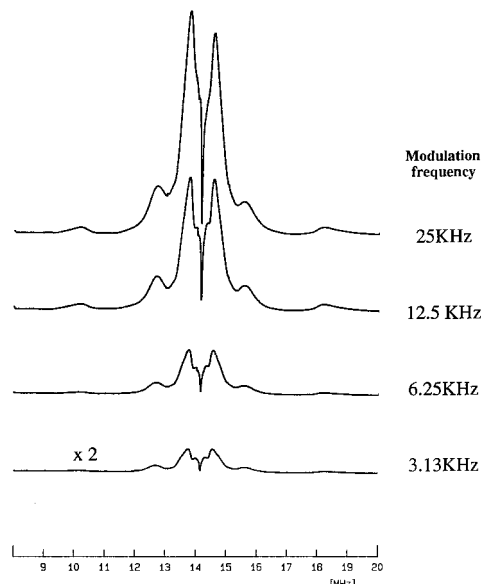
Figure 1. [1]H ENDOR amplitude spectra of Mn(II) in 30% ethylene glycol measured at 6 K with different reference phase settings. Other parameter settings: microwave frequency = 9.45 GHz, microwave power = 20 dB, rf power = 6 dB, rf modulation amplitude = 50 kHz. Magnetic field = 3277 G, sweep time = 81.96 s, and number of scans for each spectrum = 5.
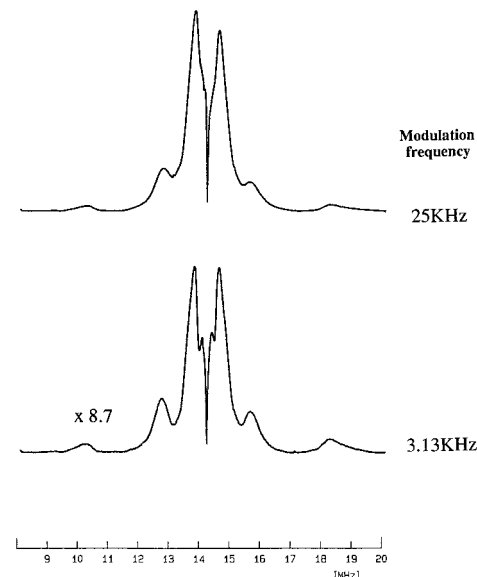

Figure 3. Dependence of ^{1}H ENDOR power spectrum on the rf modulation frequency. The ^{1}H ENDOR power spectra are used in order to separate the rf phase dependence of the ENDOR signal.

Figure 2. Power (upper panel) and phase (lower panel) spectra obtained by processing nine spectra shown in Figure 1.

Figure 4. Line-shape comparison between two power spectra obtained at 3.13 kHz (lower panel) and 25 kHz (upper panel), respectively.

equals 12.5 kHz.) By contrast, for the Mn(II) aqua system at 4 K, the ENDOR signal does not exhibit a null at any phase angle, as shown in Figure 1 for the interval 0°−160° with 20° increments. The line shape and intensity of the spectrum change gradually from one phase setting to another. The spectra obtained at reference phase settings between 180° and 340° were identical to the corresponding spectra shown in Figure 1, except that the polarity of the signals flipped.

Modulation Frequency Dependence, Power, and Phase Spectra. The ENDOR phase dependence was examined over the rf modulation frequency range from 3.13 to 25 kHz. Instead of presenting a series of spectra taken at each frequency, we used the corresponding power and phase spectra which contain the same information but are more compact. This allows us to examine the frequency response of the ENDOR amplitude and phase spectra separately. Figure 2 shows a typical pair of power and phase spectra obtained from the series of spectra shown in Figure 1. The intense spikes in the phase spectrum are artifacts

commonly seen in the low signal intensity regions.[17] Figure 3 shows that the amplitude of the ENDOR power spectra increases with the rf modulation frequency. Moreover, different hyperfine peaks exhibit different frequency dependences. This is most readily seen in Figure 4, in which the power spectra obtained at 3.13 and 25 kHz are normalized by area and compared for line-shape differences. By contrast, when ^{1}H ENDOR spectra from a homogeneously tumbling radical such as PNT are measured in this modulation frequency range, there is little change in the ENDOR amplitude.

The phase spectrum for aquo Mn(II) obtained at various frequencies approximates a step function (see Figure 2 for example at 50 kHz). A 180° phase shift occurs at the free proton Larmor frequency, corresponding to the polarity change at this point in the original ENDOR spectra (Figure 1). The phase angle above and below the free proton Larmor frequency exhibits a highly resolved structure that has a one-to-one correspondence to the original ENDOR hyperfine peaks (Figure 5). Each peak or shoulder in the ENDOR amplitude spectrum,
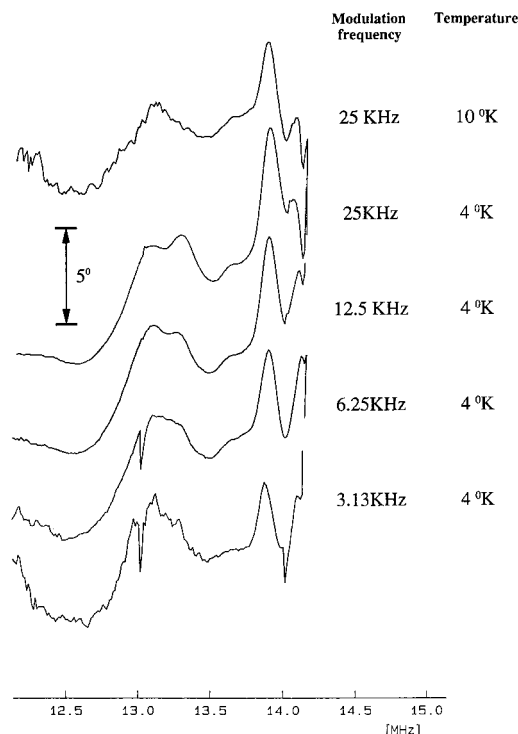
Paramagnetic Ions in Disordered Solids

J. Phys. Chem. B, Vol. 102, No. 42, 1998 **8309**
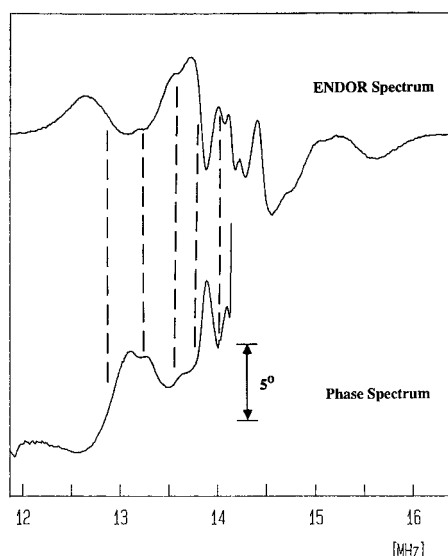
Figure 5. Upper panel: [1]H ENDOR amplitude spectrum of Mn(II) in 30% ethylene glycol measured at 6 K with reference phase set at 240°. Other parameter settings are identical to those for other spectra shown in Figure 1. Lower panel: a simple blowup of the phase spectrum shown in Figure 2. The left half part of the spectrum is off scale and omitted.

obtained at a phase that suppresses the matrix peak, corresponds to a well-resolved feature in the pure phase spectrum. The general trend in the phase spectrum reveals that the hyperfine transitions with the largest splittings exhibit the smallest rotation of their phase angles relative to the reference phase for rapidly relaxing samples. The highly resolved structure superimposed on this general trend reveals an underlying orientation dependence to the phase spectrum that originates from the anisotropy of the proton hyperfine interaction. The smallest splitting that can be resolved in the phase spectrum relative to the free proton Larmor frequency is 0.06 MHz (Figure 5). There are five features resolved in the region between 13 and 14.3 MHz.

The dependence of the phase spectrum on the rf modulation frequency is shown in Figure 6. As can be seen, the phase angle for protons with hyperfine couplings in the range 12.5−14.0 MHz increases and exhibits resolved structure. There is an increase in this phase angle difference over this range and a change of the resolved structure as the rf modulation frequency is increased from 3.13 MHz to 25 kHz. The general trend for larger phase angles is to be required for distant protons having the weakest hyperfine interactions, with higher rf modulation frequencies amplifying this increase.

Temperature Dependence. The ENDOR is known to be extremely sensitive to temperature. When the temperature is raised from 4 to above 15 K, the proton ENDOR amplitude is decreased so much that an acceptable signal-to-noise ratio (S/N) cannot be obtained in a reasonable time. At 10 K, the ENDOR amplitude drops by a factor of 3 in comparison with that obtained at 4 K. The phase spectrum at 10 K is compared with that obtained at 4 K in Figure 6. The phase angle dependence on hyperfine frequency decreases and the resolved structure changes, both resembling the response found at lower frequencies at 4 K. This behavior is consistent with more rapid relaxation at the higher temperature leading to a smaller phase angle rotation.

Rf Power Dependence. The spectra shown in Figure 1 were obtained with an rf power of 6 dB. When this power was dropped to 12 dB, the ENDOR signal intensity dropped by a factor of 2; otherwise, the spectra were the same as shown in Figure 1. The phase spectrum did not change in this range.


Figure 6. Dependence of ^{1}H ENDOR phase spectra on the rf modulation frequency and temperature.
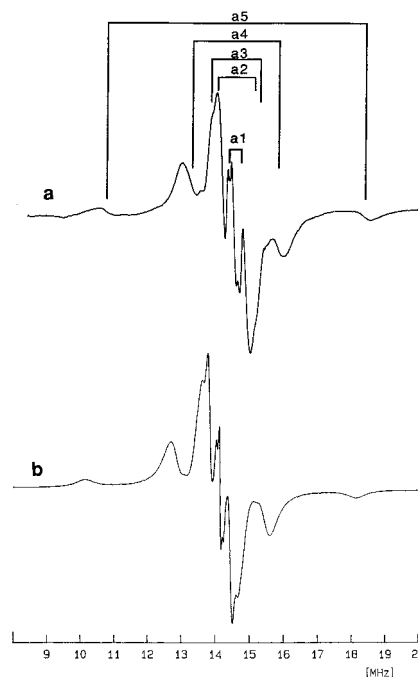
Figure 7. Upper panel: [1]H ENDOR amplitude spectrum of Mn(II) in 30% ethylene glycol measured at 6 K with reference phase set at 35° (phase optimized for spectral resolution and elimination of disordered (matrix) protons). Rf modulation amplitude = 100 kHz; other parameter settings are identical to spectra shown in Figure 1. Lower panel: simulated ^{1}H ENDOR powder spectum using parameters listed in Table 1.

Resolution of Distant Protons and Suppression of the Matrix Peak. With the knowledge gained from the phase spectrum, we can choose a phase angle that optimizes the spectral resolution in the congested matrix peak region. Figure 7a shows the ENDOR spectrum taken at phase angle 35°, where the best resolution is obtained. With the enhanced resolution it is now possible to resolve two peaks (labeled as a_2 and a_3
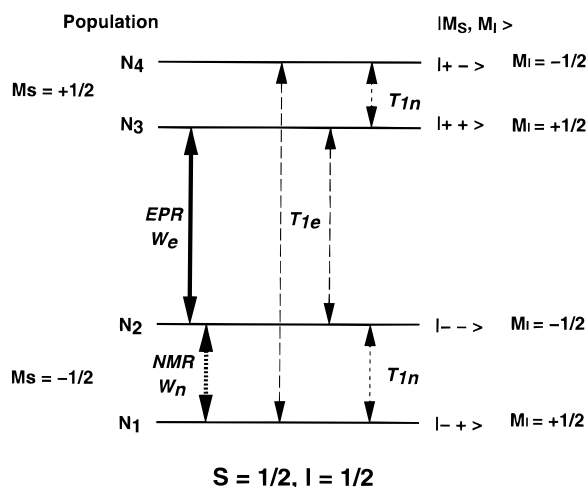
Figure 8. Energy level diagram for a $S = I = \frac{1}{2}$ system showing electron and nuclear spin relaxation path (T_{1e} and T_{1n}) and induced electron and nuclear spin transitions (W_e and W_n) that are relevent to the transient ENDOR response.

separated by 0.16 MHz) associated with the second solvation shell of water molecules. These peaks are unresolved under conditions in which the phase was selected only on the basis of optimized amplitude. In addition, a new coupling (labeled as a_1) that is separated by only 0.21 MHz from the free proton Larmor frequency is also evident. No resolution of this feature could be discerned in the amplitude-optimized ENDOR spectrum, for which the smallest coupling that could be resolved was 0.8 MHz.[14] Analysis of the spectrum will be presented in the following discussion.

Discussion

Rf Modulation Frequency and Phase Dependence of the ENDOR Signal—a Transient Phenomenon. The observed ^{1}H ENDOR signal dependence on rf modulation frequency and phase in the Mn(II) aqua system can be explained through an analysis of the transient ENDOR response for a simplified $S = \frac{1}{2}$, $I = \frac{1}{2}$ system such as given in Figure 8. We shall not present a rigorous explanation of the ENDOR, which fortunately is not needed to understand the underlying physical basis. The dynamic behavior of the model system in Figure 8 is determined by the rates of electron and nuclear spin relaxation, $1/T_{1e}$ and $1/T_{1n}$, respectively, and the rates of the induced electron and nuclear spin transitions, W_{1e} and W_{1n}, respectively.[18] The typical ENDOR experiment is done with continuous microwave irradiation of one of the electron spin transitions, say levels 2 and 3. When the rf-induced nuclear spin transition between levels 3 and 4 is turned on at time $t = 0$, the observed ENDOR response is proportional to the change in populations ($N_2 - N_3$):

$$\text{ENDOR intensity}(t) \propto (N_2 - N_3)_t - (N_2 - N_3)_0 \quad (4)$$

This response is simulated numerically, and the results obtained with two different T_{1n}/T_{1e} ratios are shown in Figure 9. As can be seen, the ENDOR signal increases rapidly immediately after the rf is switched on at $t = 0$ and reaches its maximum within a time shorter than T_{1e}. It then decays exponentially to a steady-state level. Both the decay time constant τ and steady-state level depend on T_{1e} and T_{1n}; the former can be expressed as

$$\frac{1}{\tau} = \frac{1}{T_{1e}} + \frac{1}{T_{1e} + T_{1n}} \quad (5)$$
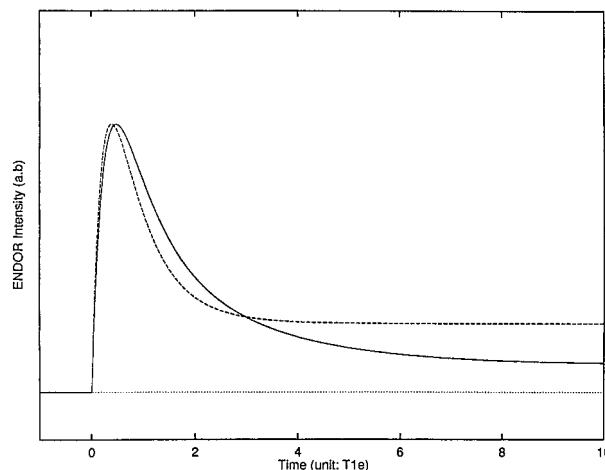
Figure 9. Transient ENDOR response of a $S = I = \frac{1}{2}$ system to a step-function rf excitation (solid line, $T_{1e}/T_{1n} = 1000$; dash-line, $T_{1e}/T_{1n} = 1$).

Now if the rf modulation frequency $f \ll 1/\tau$, then the intensity of the ENDOR signal is largely determined by the steady-state level and therefore depends little on the modulation frequency f. This is usually the case in solution ENDOR where electron spin relaxes very fast, as seen in the PNT system.[18] In the solid state and at low temperatures, however, the electron spin relaxation rate slows and the nuclear spin relaxation rate often increases, so that the rf modulation frequency may become comparable with $1/\tau$. In this case, when larger and larger modulation frequencies are used, a transient ENDOR response becomes more and more dominant in the period of signal integration, and an increase in ENDOR intensity is therefore expected. We believe that this explains the frequency dependence of the ^{1}H ENDOR spectrum of aquo Mn(II). From the frequency dependence, the electron spin relaxation time T_{1e} is estimated to be $10^{-3}-10^{-4}$ s in the temperature range from 4 to 10 K. This value is in agreement with a report in the literature.[19]

The dependence of the transient ^{1}H ENDOR response on T_{1n} (eq 5 and Figure 9) can explain the ENDOR phase pheonomena we observed in the Mn(II) aquo system. The relaxation of a proton nuclear spin in a paramagnetic transition metal center is a well-studied subject.[20] The proton spin relaxation rate depends on the proton–electron spin separation via the magnetic dipolar interaction. This interaction leads to the prediction of an r^{-6} distance dependence for the nuclear spin relaxation rate:[20]

$$\frac{1}{T_{1n}} \propto \left(\frac{H_e}{H_0}\right)^2 \frac{1}{T_{1e}} \propto \frac{1}{r^6} \quad (6)$$

where H_0 is the external magnetic field, H_e is the electron magnetic dipolar field strength at the proton site, and r is the proton–metal separation. An additional contribution due to spin diffusion between fast relaxing protons and slowly relaxing protons diminishes the distance dependence of the proton relaxation rate,[20] but the overall trend should remain. Therefore, for protons in the first coordination shell, T_{1n} is expected to be comparable to T_{1e}, whereas for distant matrix protons, T_{1n} can be several orders of magnitude smaller than T_{1e}. The transient ENDOR response from these two types of protons is thus very different, as is illustrated in Figure 8. In the time domain, this difference is manifested as a superposition of the two decay curves; in the frequency domain, this appears as a phase angle rotation of the ENDOR amplitude response from these two types of protons.

Paramagnetic Ions in Disordered Solids

J. Phys. Chem. B, Vol. 102, No. 42, 1998 **8311**

TABLE 1: ^{1}H Hyperfine Tensors (MHz), Line Shapes, and Mn−H Distances for Aquo Mn(II)^a in Frozen Glass at 6 K Derived by DEEP Spectroscopy^{a,b}

A_{per}/MHz	A_{par}/MHz	$\delta\nu$/MHz	W	solvation shell	point−dipole distance/Å	distance from MD simulation^c
2.70 (a_4)	7.95 (a_5)	0.34	1.200	first	2.90	2.9
1.05 (a_3)	2.10	0.13	0.180	second	4.37	4.2
0.68 (a_2)	1.36	0.13	0.400	second	5.05	4.8
0.21 (a_1)	0.42	0.06	0.024	third	7.47	7.5 (300 K)
0.00	0.00	0.06	0.009	matrix	NA	NA

^{a} W = weighting factor; $\delta\nu$ = line width. ^{b} MnCl$_2$ in 30−50% ethylene glycol glass. ^{c} Reference 14.

The transient ENDOR phenomenon has long been recognized[21,22] and has been utilized to increase the ENDOR sensitivity by employing novel detection schemes.[21−25] However, we are unaware of any published work in which the transient phenomena are used to increase the ENDOR spectral resolution. The present work demonstrates the utility of this approach with isotropic spin systems such as high-spin Mn(II). One pitfall of the approach is the decrease in signal intensity that occurs when the difference in phase angle rotation for different protons is small. This S/N problem can be circumvented by capturing both the power and phase spectral information simultaneously by utilizing a quadrature detection scheme. This approach is commonly adopted in NMR experiments.

Hyperfine Assignments, Spectral Simulation, and Solvation Structure. A simulation of the phase-optimized ENDOR spectrum shown in Figure 7a is given in Figure 7b. It was performed in order to aid assignment of the transitions and to extract the most accurate hyperfine tensor elements. An accurate simulation could be achieved assuming four sets of hyperfine tensors with axial symmetry ($A_{\parallel} = -2A_{\perp}$); variable line widths and variable relative weights are present in a randomly oriented sample (Table 1). The best simulations required inclusion of an isotropic Gaussian peak at the proton Larmor frequency assigned to residual free protons.

In our previous report, hyperfine splittings a_5 and a_4 (refer to Figure 7a and Table 1) were assigned to the parallel and perpendicular components, respectively, of an axial hyperfine tensor for the first shell protons.[14] These assignments are in good agreement with many other reports.[13,26] The spherical symmetry of the Mn(II) high-spin 3d^5 electronic distribution (^{6}A ground state) and the absence of significant spin density on the water ligands is responsible for the axial nature of the hyperfine tensor. The Mn···H distance calculated from this assuming the magnetic point-dipole model with $S = ^1/_2$ and $I = ^1/_2$ is 2.90 Å, in excellent agreement with neutron diffraction data and ENDOR on single crystals.[6,13]

Hyperfine couplings a_3 and a_2 could not be separated in our previous measurements using conventional ENDOR; only a single broad peak was observed which was assigned to the perpendicular component of an axial hyperfine tensor for water protons in the second shell. The resolution into two distinct peaks indicates that either the second shell of water molecules must possess two different sites with distinct H···Mn distances or that the ethylene glycol cosolvent contributes to the spectrum (vide infra). Assuming that the a_2 and a_3 couplings arise from the perpendicular hyperfine tensor component of two different tensors, as supported by the spectral simulation (Figure 7b), we calculated the Mn···H distances using the point-dipole model for the Mn(II) spin density and $S = ^1/_2$, corresponding to the transition within the inner doublet $M_s = \pm^1/_2$. The distances obtained are 4.37 and 5.05 Å (Table 1). This provides the first experimental evidence that we are aware of for the existence of substructure within the second solvation shell of water

molecules and is in agreement with an earlier molecular dynamics prediction (Table 1).[14]

The smallest coupling a_1 in Figure 7 and Table 1 (0.21 MHz), is assigned to either water protons or ethylene glycol hydroxyl protons in the third coordination shell. Assuming that the 0.21 MHz coupling arises from the perpendicular hyperfine tensor component, as supported by the spectral simulation result in Figure 7b, it would correspond to a Mn···H distance of 7.5 Å. This distance is quite reasonable for protons in a third solvation shell of water molecules (or possibly hydroxyls from ethylene glycol) that are hydrogen-bonded to the second shell water molecules, based on molecular modeling.[14]

To test whether any of the observed hyperfine couplings arise from protons of the ethylene glycol cosolvent instead of from water molecules, we repeated the experiment replacing the 30% ethylene glycol with ethylene glycol-d_6. Comparison of parts a and b of Figure 10 shows that all of the hyperfine couplings are identical, but the intensity of the spectrum is weaker in the deuterated sample. Since the number of scans and Mn^{2+} concentrations are the same, the lower intensity indicates that there could be fewer protons contributing to the spectrum and fewer Mn(II) ions with ordered hydration shells (e.g., more disorder) or that the proton spin diffusion rate is affected so as to decrease the ENDOR effect. The invariance of the resolved spectral features to deuteration of the ethylene glycol proves that there are no ethylene backbone protons responsible for the ENDOR features that are observable using the phase angle approach. Because of the exchangeability of the hydroxyl protons of ethylene glycol, we cannot exclude the possibility that hyperfine interaction with these protons may contribute to the third shell. However, we argue that they will not have any contribution to at least the first two shells, because otherwise we should see couplings to the backbone protons also. We examined the ENDOR spectra as a function of ethylene glycol concentration in the range 30−50% (glassing was observed in all cases) and found no effect on the spectral features. This indicates that water solvation around the Mn^{2+} is thermodynamically favored over ethylene glycol, as is intuitively expected based on elementary considerations of solvation energies.

We did not observe couplings larger than 9 MHz in our aquo Mn(II) sample. This is in contrast to what has been observed by Tan et al. in a similar system (Mn(II) in a 1:1 mixture of 50 mM pH 7 Hepes buffer and glycerol), where a number of low-intensity larger couplings (12.2, 22.2, and 36.4 MHz) were seen by both CW (with Zeeman field modulation) and pulsed ENDOR. All of these peaks were assigned to the first shell protons, but arising from different noncentral EPR transitions $|M_s| > ^1/_2$.[26] In our experiments, the largest coupling observed is $a_5 = 7.95$ MHz. According to the line shape of this pair of transitions and the simulation result (Figure 7b), it could be assigned to a parallel hyperfine tensor component of the first shell proton. We attributed this to hyperfine coupling within the $M_s = \pm^1/_2$ manifold because this assumption correctly

8312 *J. Phys. Chem. B, Vol. 102, No. 42, 1998*

Zheng and Dismukes
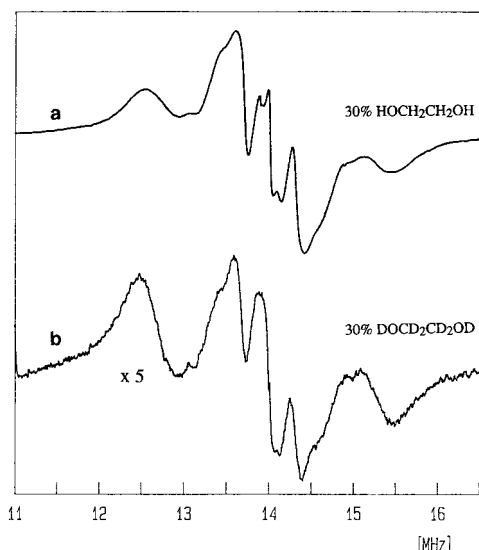
Figure 10. Comparison of two ^{1}H ENDOR amplitude spectra obtained from Mn(II) aquo with 30% ethylene glycol (upper trace) and 30% perdeuterated ethylene glycol (lower trace).

accounts for the Mn···H distance. In principle, noncentral EPR transitions could give rise to a series of redundant ENDOR peaks from a single-proton hyperfine component, but the intensities of these redundant ENDOR transitions must be proportional to the intensities of the corresponding noncentral EPR transitions, which in turn are determined by the magnitude of the zfs parameters. Mn(II) with $S = {}^5/_2$ exhibits both quadratic and quartic zfs terms that split the M_s manifolds even in cubic symmetry environments. A study on the Mn(II) noncentral EPR transitions at 9 and 33 GHz has shown that, with a typical Mn-(II) zero-field splitting D value of only 66 G, the noncentral transitions are 1−2 orders of magnitude weaker than the central ($M_s = {}^1/_2$ to $M = -{}^1/_2$) transition centered around $g = 2$.[15] The spin relaxation rate is also faster in the noncentral M_s manifolds and thus will not give rise to efficient CW ENDOR detection under conditions that optimize detection of the slower relaxing central M_s transition. These considerations emphasize that the use of the phase spectrum to discriminate selectively ENDOR transitions with different T_{1e} values provides an important method for spectral simplification by elimination of redundant ENDOR transitions from higher M_s manifolds.
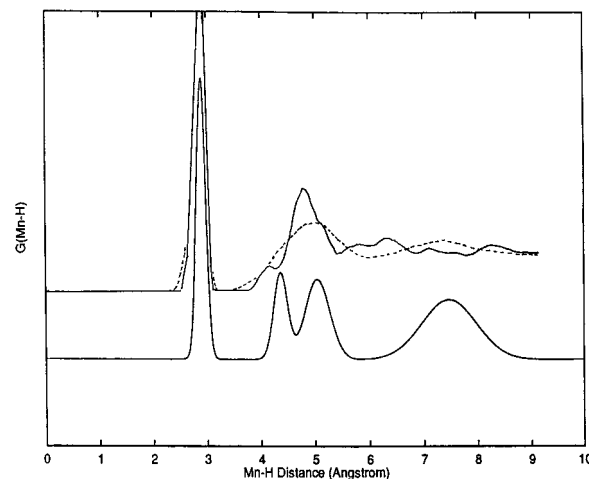
Construction of the Mn−H Radial Distribution Function. To help visualize the Mn(II) hydration shell structure as revealed by our ENDOR data and to facilitate comparison to data obtained by other methods including molecular dynamics simulation and X-ray and neutron diffractions, we have calculated the experimental Mn···H radial distribution function from our ENDOR data in Figure 11. To do this, it is assumed that proton distribution in each hydration shell can be described by a Gaussian function:

$$G(r) = C \exp\left[-\left(\frac{r - r_0}{\delta r}\right)^2\right] \tag{7}$$

where r is the Mn−H separation and r_0 corresponds to the central position of the hydration shell as determined from the ENDOR spectral simulation (Table 1). δr is obtained through the corresponding ENDOR line width $\delta\nu$ (Table 1) with the following equation.

$$\frac{\delta r}{r_0} = \frac{\delta\nu}{3\nu} \tag{8}$$

Figure 11. Mn−H radial distribution function: (bottom) constructed according to the ^{1}H DEEP data from the Mn(II) aquo system; (top) molecular dynamics simulation at 300 (dashed) and 50 K (solid) from ref 14.

This treatment assumes that the observed ENDOR line width is due entirely to the proton distribution in a hydration shell; therefore, the calculated value of δr corresponds to its upper limit. The normalization constant C in eq 7 is obtained by setting the integral of the distribution function in eq 7 equal to the number of protons in the shell (N):

$$\int_0^\infty 4\pi r^2 G(r)\, dr = N \tag{9}$$

Unfortunately, the ENDOR intensity does not tell us the proton population in each hydration shell. Hence, this is an undetermined parameter. We have chosen six water molecules in the first shell, 20 in the second, and 50 in the third shell in our calculation. The 20 water molecules in the second shell are further partitioned into two observed subshells according to the intensity ratio (0.18:0.40) of the their ENDOR lines(Table 1); this is a reasonable treatment since the relaxation properties of the protons in the two subshell are expected to be similar. From the calculated radial distribution function in Figure 11 the three ordered hydration shells of Mn(II), with two well-resolved subshells in the second shell, are clearly seen. However, the relative peak intensities of each shell have to be viewed in light of assumptions we made above.

Molecular Dynamics Simulations. In our previous work we presented results from classical molecular dynamics simulations of Mn(II) ions solvated by 212 water molecules.[14] The simulation used a widely distributed three-point flexible water model with electrostatic and van der Waals interactions to Mn-(II). The MD simulation results are reproduced in Figure 11 and tabulated in Table 1 for comparison to the ENDOR calculated radial distribution function described above. The MD results predicted the presence of substructure in the second solvation shell and the presence of an ordered third shell before the high-resolution ENDOR data were available. The equilibrium Mn−H radial distribution function computed at 50 K revealed the first shell of water protons at 2.9 Å (6 molecules), a structured second solvation shell with minor peak at 4.2 Å (2−3 molecules), and a major peak at 4.8 Å (16−15 molecules) and longer range interactions exhibiting modest preference for Mn−H distances at 6.4 and 8.4 Å. The radial distribution function did not change at lower temperatures, but at 300 K the distribution broadens to encompass 22 molecules in a larger more disordered second shell peaking at 5.0 Å, while a broad third shell emerges at 7.4 Å. The MD prediction of the resolved

Paramagnetic Ions in Disordered Solids

J. Phys. Chem. B, Vol. 102, No. 42, 1998 **8313**

structure in the second shell and the presence of an ordered third shell could not be confirmed experimentally in the previous work using the ENDOR amplitude spectrum alone. These persistent features of the simulation can now be confidently assigned to ordered shells of water molecules that are close to the distances found using DEEP spectroscopy (Table 1). Unfortunately, the ENDOR method does not permit determination of the number of nuclei with reliable accuracy.

Three Ordered Hydration Shells. DEEP spectroscopy allows one to see three ordered hydration shells around dilute solutions of aquo Mn(II) ions. The existence of a second hydration shell was also inferred from analysis of X-ray diffraction data obtained from a 2 M $MnSO_4$ solution[5] and EXAFS data from 0.1 M $MnCl_2$ solution.[27] To our best knowledge, the third hydration shell of ordered water molecules around Mn(II) has never been observed before. This absence of earlier detection might be caused by a loss of long-range hydration structure with increasing ion concentration. Since ion−solvent interactions are electrostatic in nature, the force field created by a Mn(II) ion to orient the surrounding water molecules will be disturbed by other nearby ions, thus decreasing the effective field range. The effect of ion concentration has been demonstrated before by molecular dynamics simulation in NaCl solutions.[28] It was found that decreasing the NaCl concentration from 2.2 to 0.55 M induces the formation of significant order in the second hydration shell.

Future Perspectives

In summary, we have presented an application of phase modulation spectroscopy to ENDOR experiments which enable enhanced resolution based on the distance dependence of electron spin−nuclear spin cross relaxation effects. Distance-enhanced ENDOR phase (DEEP) spectroscopy was demonstrated and applied to simplification of the free proton matrix and discovery of long-range order from hydration shells around aquo Mn(II). This method should be generally applicable to isotropic spin systems, including Gd(III) which is used as an MRI contrast agent. We have observed DEEP in solutions of Cu(II) and $Mn_2O_2(bipy)_4{}^{3+}$ also, where the phase discrimination effect is less though, perhaps due to larger *g* and hyperfine anisotropies and covalency. It is hoped that the methodology presented here could find usage in the ENDOR investigations of other chemical and biological systems.

References and Notes

(1) Conway, B. E. *Ionic Hydration in Chemistry and Biophysics*; Elsevier Scientific Publishing Company: Amsterdam, 1981.

(2) Krestov, G. A.; Novosyolov, N. P.; Perelygin, I. S.; Kolker, A. M.; Safonova, L. P.; Ovchinnikova, V. D.; Trostin, V. N. *Ionic Solvation*.

(3) Nicholls, D. G. *Bioenergetics*; Academic Press: London, 1982.

(4) Narten, A. H.; Vaslow, F.; Levy, H. A. *J. Chem. Phys.* **1973**, *58*, 5017−5023.

(5) Licheri, G.; Paschina, G.; Piccaluga, G.; Pinna, G. *J. Chem. Phys.* **1984**, *81*, 6059−6063.

(6) Enderby, J. E. In Chem, A. R. P., Ed.; *Annual Reviews*; 1983; Vol. 34, pp 155−185.

(7) Munoz-Paez, A.; Pappalardo, R. R.; Marcos, E. S. *J. Am. Chem. Soc.* **1995**, *117*, 11710−11720.

(8) Nightinggale, E. R. *J. Phys. Chem.* **1959**, *63*, 1381−1387.

(9) Hurst, G. C.; Henderson, T. A.; Kreilick, R. W. *J. Am. Chem. Soc.* **1985**, *107*, 7294.

(10) Hutchison, C.; McKay, D. B. *J. Chem. Phys.* **1977**, *66*, 3311.

(11) Yim, M. B.; Makinen, M. W. *J. Magn. Reson.* **1986**, *70*, 89.

(12) Mustafi, D.; Makinen, M. *Inorg. Chem.* **1988**, *27*, 3360.

(13) DeBeer, R.; DeBoer, W.; Van't Hof, C. A.; Van Ormondt, D. *Acta Crystallogr.* **1973**, *B29*, 1473.

(14) Sivaraja, M.; Stouch, T. R.; Dismukes, G. C. *J. Am. Chem. Soc.* **1992**, *114*, 9600−9603.

(15) Zhang, Y. P.; Buckmaster, H. A. *J. Magn. Reson. A* **1993**, *102*, 152−159.

(16) Halkides, C. J.; F., B. B.; Gerfen, G. J.; Farrar, C. T.; Carter, P. H.; Ruo, B.; Evans, D. A.; G., G. R.; Singel, D. J. *Biochemistry* **1996**, *35*, 2194−12200.

(17) Shimoyama, Y.; Wateri, H. *J. Chem. Phys.* **1986**, *84*, 3688−3693.

(18) Kurreck, H.; Kirste, B.; Lubitz, W. *Electron Nuclear Double Resonance Spectroscopy of Radicals in Solution*; VCH: Weinheim, 1988.

(19) Horak, J. B.; Nolle, A. W. *Phys. Rev.* **1967**, *153*, 372−378.

(20) Abragam, A. *The Priciples of Nuclear Magnetism*; Clarendon Press: Oxford, 1961; pp 379−386.

(21) Feher, G. *Phys. Rev.* **1959**, *114*, 1219.

(22) Seidel, H. *Z. Phys.* **1961**, *165*, 239−252.

(23) Scholes, C. P. In *Multiple Electron Resonance Spectroscopy*; Dorio, M. M., Freed, J. H., Eds.; Plenum Press: New York, 1979; pp 297−328.

(24) Bruggemann, W.; Niklas, J. R. *J. Magn. Reson. A* **1994**, *108*, 25−29.

(25) Hoganson, C. W.; Babcock, G. T. *J. Magn. Reson. A* **1995**, *112*, 220−224.

(26) Tan, X. L.; Bernardo, M.; Thomann, H.; Scholes, C. P. *J. Chem. Phys.* **1993**, *98*, 5147−5157.

(27) Bealey, B.; McAuliffe, C. A.; Smith, S. P. B.; White, E. W. *J. Phys.: Condens. Matter* **1991**, *3*, 7919.

(28) Vogel, P. C.; Heinzeiger, K. *Z. Naturforsch.* **1976**, *31A*, 476.